




THE UNIVERSITY
of ADELAIDE



Deutsches Zentrum
für Luft- und Raumfahrt



**EXPERIMENTAL INVESTIGATION OF HIGH
FREQUENCY COMBUSTION INSTABILITY
IN CRYOGENIC OXYGEN-HYDROGEN
ROCKET ENGINES**

Justin S. Hardi

Experimental Investigation of High Frequency Combustion Instability in Cryogenic Oxygen-Hydrogen Rocket Engines

Justin S. Hardi

School of Mechanical Engineering
The University of Adelaide
South Australia 5005
Australia

A thesis submitted in fulfilment of the requirements
for the degree of Ph.D in Aerospace Engineering
in June 2012

Contents

Contents	ii
List of figures	vi
List of tables	x
Glossary	xi
Abstract	xiii
Declaration of originality	xv
Acknowledgements and disclaimer	xvii
1. Introduction	1
2. Background	3
2.1 Launch vehicles	3
2.2 Rocket propulsion	4
2.3 Liquid propellant rocket engines	6
2.3.1 Liquid propellant rocket engine performance.....	7
2.3.2 Liquid propellants.....	8
2.3.3 Injector types	9
2.3.4 Propellants.....	10
2.4 Oxygen-hydrogen propellant combination	11
2.4.1 Hydrogen fuel	11
2.4.2 Liquid oxygen oxidiser	12
2.4.3 Supercritical conditions.....	12
2.5 Combustion chamber processes.....	14
2.5.1 Propellant injection	15
2.5.2 Atomisation of liquid propellants.....	15
2.5.3 Secondary atomisation	16
2.5.4 Vaporisation.....	16
2.5.5 Combustion.....	16
2.6 Combustion instability	17
2.6.1 Characterising combustion instability	17
2.6.2 High frequency combustion instability	18
2.6.3 Driving mechanisms of instabilities.....	19
2.6.4 Controlling combustion instability	21
3. Literature survey	27
3.1 Investigations up to 1972	27
3.2 Investigations from 1972 to 1995.....	36
3.3 High pressure research.....	36
3.4 Recent HF instability research	41
3.4.1 Non-reacting flows.....	41
3.4.2 Reacting flows	45

3.5	Summary	51
4.	Combustor development.....	53
4.1	Experimental combustor review	53
4.1.1	Historical overview	53
4.1.2	CRC	55
4.1.3	MIC and VHAM	57
4.1.4	Pennsylvania State University rectangular combustor.....	59
4.1.5	Purdue University rectangular combustor.....	59
4.1.6	Summary.....	60
4.2	New combustor specifications.....	60
4.2.1	Operating conditions	60
4.2.2	Test facility.....	61
4.2.3	Injector	62
4.3	Conceptual design.....	63
4.3.1	Concept 1: High pressure CRC	63
4.3.2	Concept 2: Rectangular chamber	64
4.3.3	Concept 3: Excitation segment for BKB.....	65
4.3.4	Concept 4: Ring resonator segment for BKB.....	66
4.3.5	Concept 5: Twin resonator segment for BKB	68
4.3.6	Concept selection	69
4.4	New rectangular combustor: BKH.....	70
4.4.1	BKH concept overview.....	70
4.4.2	Combustion chamber acoustics.....	71
4.4.3	Primary injector	72
4.4.4	Secondary injection.....	73
4.4.5	Diagnostics	75
4.4.6	Optical access.....	76
4.4.7	Excitation system	76
5.	Experimental techniques.....	81
5.1	Test operations.....	81
5.1.1	Test facility.....	81
5.1.2	Test campaigns.....	81
5.1.3	Hardware integration.....	82
5.1.4	Test runs	82
5.1.5	Test sequences	84
5.2	Diagnostics and data acquisition.....	85
5.3	Optical diagnostics	86
5.3.1	OH* chemiluminescence imaging	86
5.3.2	Shadowgraph imaging	88
5.3.3	OH* chemiluminescence recording with photomultipliers	88
5.4	Campaigns 1 and 2: initial hardware testing	88
5.4.1	Test type 1; clean configuration	89
5.4.2	Test type 2; clean configuration with optics	90
5.4.3	Test type 3; with excitation and optics	92
5.5	Campaigns 3 and 4: excitation and optics with ambient hydrogen	95
5.5.1	Test type 4; with excitation.....	96
5.5.2	Test type 5; with excitation and optics	97
5.6	Campaign 5: excitation and optics with cryogenic hydrogen.....	101
5.6.1	Test type 6; cold flow with excitation.....	101
5.6.2	Test type 7; with excitation and optics	101
5.7	Summary of achieved operating conditions	102
6.	Acoustic characterisation	103

6.1	Finite element acoustic model.....	103
6.2	Spectrum characterisation	105
6.3	System modification: acoustic baffle	110
6.4	Acoustic excitation	114
6.4.1	Spectrum characterisation	114
6.4.2	Low frequency instability.....	117
6.4.3	Excitation amplitude.....	118
6.5	Combustion response	121
6.6	Injection coupling	124
6.7	Summary	128
7.	Flame response	129
7.1	Review of flame response studies	129
7.2	Flame structure	131
7.3	Flame displacement.....	135
7.4	Dynamic OH* emission response	137
7.5	Dynamic response to transverse excitation	141
7.6	Dynamic response to longitudinal excitation.....	146
7.7	Photomultiplier response measurements.....	149
7.8	Summary.....	150
8.	Oxygen core response	153
8.1	Review of oxygen core studies	153
8.2	Oxygen core structure.....	155
8.3	Dynamic response to transverse excitation	161
8.4	Intact core length measurements.....	164
8.5	Secondary atomisation.....	170
8.6	Summary.....	173
9.	Conclusions	175
10.	Outlook.....	177
11.	References	179
Appendix A.	Twin resonator segment design study	189
A.1	Twin resonator segment geometry.....	189
A.2	Internal flow.....	191
A.3	Secondary injection	194
A.4	Water condensation	199
A.5	Manufacture feasibility study.....	199
Appendix B.	BKH dimensions.....	201
B.1	Combustor drawings	201
Appendix C.	Modified secondary nozzle	205
C.1	Round nozzle	205

C.2	Double sine nozzle	206
Appendix D. List of articles resulting from this work		209
D.1	Journal articles	209
D.2	Conference papers.....	209

List of figures

Figure 2.1: Heavy launch vehicles using LPREs; (from left to right) Ariane 5 (Arianespace 2012), Space Shuttle (NASA 2007), Soyuz (Arianespace 2012), and Delta IV (Boeing 2007).	4
Figure 2.2: Schematics of liquid, solid and hybrid rocket propulsion systems (Image credit: Andrew Sysouphat 2005).	5
Figure 2.3: Ariane 5 launch vehicle highlighting the main components (modified from DKimages 2007).	6
Figure 2.4: Schematic diagram of the main components of a liquid rocket (Sutton & Biblarz 2001, p.8).	7
Figure 2.5: Schematic diagrams of several liquid rocket injector types (Sutton & Biblarz 2001, p.274).	9
Figure 2.6: The injector assembly of the J-2 engine (left) (Dykema 1972, p.360), and an illustration of a simple shear coaxial injector with no recess (right).	10
Figure 2.7: Pressure balance on a typical thrust chamber (Sutton & Biblarz 2001, p.33).	13
Figure 2.8: Phase diagram indicating transcritical injection of oxygen, c_p values from Younglove (1982).	13
Figure 2.9: Critical mixing lines for three binary systems (Mayer & Smith 2004, p.8).	14
Figure 2.10: Comparison of coaxial injection at subcritical and supercritical pressures (Mayer & Tamura 1996, p.1146).	15
Figure 2.11: Typical traces of chamber pressure with time for smooth and rough combustion (Sutton & Biblarz 2001, p.349).	18
Figure 2.12: Characteristics of transverse modes.	19
Figure 2.13: Cutaway sketch of a thrust chamber showing the injector-face baffle (Harrje & Reardon 1972, p.157).	23
Figure 3.1: Cutaway sketch of the variable-angle sector motor (Crocco, Harrje & Reardon 1962, p.368).	28
Figure 3.2: Droplet stream response to external acoustic forcing for three parallel jets (images of better quality unavailable) (Miesse 1955, p.527).	29
Figure 3.3: Oxygen jet length reduction during transverse mode acoustic instability (Heidmann 1965b, p.10).	32
Figure 3.4: Response factor curve for n-heptane based on vaporisation parameters (Heidmann & Wieber 1966a, p.8).	33
Figure 3.5: Response curves for heptane and oxygen (Heidmann & Wieber 1966b, p.17).	34
Figure 3.6: Flame and flow field imaging of the near injector region of a reacting flow of LOx/H ₂ at 45 bar chamber pressure (modified from Mayer et al. 1996).	39
Figure 3.7: Comparison of back-lit shadowgraph imaging of the flow field for (a) subcritical and (b) supercritical chamber pressures (modified from Mayer et al. 1996).	40
Figure 3.8: Interaction of acoustic waves with a single LN ₂ jet injected into GN ₂ under subcritical conditions (Chehroudi et al. 2003, p.19).	42
Figure 3.9: Interaction of acoustic waves with a coaxial jet of LN ₂ /GN ₂ under supercritical conditions (Chehroudi et al. 2003, p.26).	43
Figure 3.10: Consecutive frames from high-speed shadowgraph imaging of acoustic forcing of a coaxial nitrogen jet under subcritical, near-, and supercritical conditions (Davis & Chehroudi 2006, p.5).	44
Figure 3.11: V-profile pressure ramping test (Smith et al. 2004, p.11).	45
Figure 3.12: Instantaneous and time- averaged OH* emission images (in false colour) from the MIC, without (left column) and with (right column) 1T mode excitation (Richecoeur 2006, p.78).	48
Figure 3.13: Configuration of the multi-element rectangular combustor (top, cross-sectional view) with the first and second mode shapes superimposed (Marshall et al. 2006a, p.3).	49
Figure 3.14: Purdue University rectangular combustor with central swirl coaxial study element (Wierman, Nugent & Anderson 2011, p.3).	50
Figure 4.1: Streak photography of a rotating 1T mode instability (Tischler & Male 1956).	54
Figure 4.2: Working principle of small rocket combustor with intermittent nozzle modulation (Lecourt & Foucaud 1987, p.2).	55
Figure 4.3: CRC combustor for HF research (Knapp, Farago & Oschwald 2007, p.3).	56
Figure 4.4: Pressure fields in the DLR combustor with the secondary nozzle in the 180° position (left) and the 90° position (right) (Knapp, Farago & Oschwald 2007, p.3).	56
Figure 4.5: Illustration of the MIC configuration with three injection elements (left, middle), and a photograph of the five-element version of the injector (right) (modified from Richecoeur 2006).	58
Figure 4.6: Illustration of the MIC equipped with the VHAM (left) (Méry et al. 2008), and a numerically calculated 1T mode pressure distribution (right) (Richecoeur 2006, p.246).	59
Figure 4.7: Penta-injector pattern and relative acoustic field orientation.	63
Figure 4.8 High pressure CRC concept (internal geometry).	63
Figure 4.9: Rectangular combustor concept (internal geometry).	64
Figure 4.10: First three acoustic mode shapes for the MIC illustrating the influence of the secondary nozzle on mode symmetry (Richecoeur 2006, p.57).	64
Figure 4.11: Experimental combustor BKB (Suslov et al. 2005, p.3).	65
Figure 4.12: BKB with excitation segment concept (internal geometry).	66
Figure 4.13: BKB with ring resonator concept (internal geometry).	66

Figure 4.14: Numerically calculated BKB-ring resonator chamber resonance modes.....	68
Figure 4.15: Twin resonator segment concept (internal geometry).	68
Figure 4.16: Twin resonator segment resonance modes of interest.....	69
Figure 4.17: BKH combustor concept.....	70
Figure 4.18: Internal volume of the BKH combustion chamber.	71
Figure 4.19: Pressure distributions for the resonance modes of a simple rectangular volume as listed in Table 4.	72
Figure 4.20: BKH Penta-injector pattern dimensions.....	73
Figure 4.21: Injector faceplate showing secondary hydrogen injection arrays, and the desired influence on the flow field.	74
Figure 4.22: Dynamic pressure sensor locations and model names in BKH.....	75
Figure 4.23: Optical access windows and dummy windows.....	76
Figure 4.24: Modal analysis results showing the influence of secondary nozzle length on the 1T mode structure. The numerical mode calculations were conducted in FlexPDE using a sound speed of 1712 m/s. The primary and secondary nozzle exit sizes have been scaled for two-dimensionality.	77
Figure 4.25: Photographs of the excitation system installed on BKH.	78
Figure 4.26: The excitation system on BKH with housing installed.	79
Figure 5.1: European Test Facility 'P8' for cryogenic rocket engine research.....	82
Figure 5.2 BKH integration with the P8 test facility.....	83
Figure 5.3: Photographs of the test cell during a BKH test run, taken from the D68 control building.....	84
Figure 5.4: Emission spectrum from a LOx/H ₂ sub-scale combustor.....	87
Figure 5.5: BKH configuration for test type 1; clean configuration.....	89
Figure 5.6: Example test sequence for test type 1; staged ROF.....	90
Figure 5.7: BKH configuration for test type 2; clean configuration with optics.....	90
Figure 5.8: Initial optical setup for campaigns 1 and 2.....	91
Figure 5.9: Example test sequence for test type 2; staged ROF with optics.....	91
Figure 5.10: Example shadowgraph images from test type 2, for a 40 bar operating condition with ROF = 2 (left), and with ROF = 6 (right).	92
Figure 5.11: BKH configuration for test type 3; with excitation and optics.....	93
Figure 5.12: Exciter wheel modification.....	94
Figure 5.13: Example test sequence for test type 3; uncontrolled excitation ramp with optics.....	94
Figure 5.14: Example shadowgraph images from off-resonance conditions in test type 3, at 50 bar with ROF = 6 (left), and 60 bar with ROF = 6 (right).	95
Figure 5.15: Example instantaneous raw OH* images from test type 3, taken from off-resonance excitation at t = +4 s (a), and 1T mode excitation at t = +5.3 s (b).	95
Figure 5.16: Video frames during sequence failure, and resulting hardware damage.....	96
Figure 5.17: Example test sequence for test type 4; controlled excitation ramp.....	97
Figure 5.18: Modified optical setup.....	97
Figure 5.19: Photos of the modified optical setup.....	98
Figure 5.20: Example shadowgraph images from a test at 40 bar with GH ₂ (a), and a test at 60 bar with GH ₂ (b).	99
Figure 5.21: Example test sequence for test type 5; with excitation and optics.....	99
Figure 5.22: Instantaneous raw OH* images from the test in Figure 5.21 during off-resonance (a) and 1T-mode excitation (b).	100
Figure 5.23: Example spectrogram from a photomultiplier.....	100
Figure 5.24: Example shadowgraph images from a test at 40 bar with LH ₂ (a), and at 60 bar with LH ₂ (b).....	101
Figure 5.25: Sensing areas of the photomultipliers for test type 7.....	102
Figure 5.26: Achieved operating conditions of BKH.....	102
Figure 6.1: Finite element model of BKH showing (a) the fluid property groups (for the configuration with secondary nozzle), and (b) the meshed model (without secondary nozzle).	104
Figure 6.2: PSD spectrum of dynamic pressure signals from PCCdyn2 (a), and from PIHdyn (b). PIHdyn is shown with indicated mode frequencies as calculated using the FE model.	106
Figure 6.3: Example FE-calculated pressure distributions of some secondary H ₂ manifold acoustic modes.....	107
Figure 6.4: PSD of PCCdyn2 with analytical and FE calculated mode frequencies indicated (a), and with actual chamber resonance modes identified as 'selected' (b).....	108
Figure 6.5: Mode identification by sensor phase analysis for the 1L mode at 3200 Hz (a), 1T mode at 4370 Hz (b), and 1L1T mode at 5370 Hz (c).....	109
Figure 6.6: PSD of PCCdyn2 with FE calculated mode frequencies indicated for both ideal sound speed and sound speed corrected for c* combustion efficiency.	110
Figure 6.7: Design of the acoustic baffle for the secondary H ₂ manifold. Also shown is the geometry of the FE model with the baffle included.....	111
Figure 6.8: Results with the acoustic baffle installed in the secondary H ₂ manifold; (a) PSD of PIHdyn without baffle (repeated here for convenience), (b) PSD of PIHdyn with baffle, and (c,d) the corresponding PSD of PCCdyn1.....	113
Figure 6.9: Power spectra comparing primary combustion chamber modes with and without secondary nozzle installed....	114

Figure 6.10: FE-calculated pressure distributions for the 1T mode; (a) without, and (b) with the secondary nozzle installed.	114
Figure 6.11: Mode identification by sensor phase analysis with on-resonance excitation for the 1L mode (a), 1T mode (b), and 1L1T (c).....	115
Figure 6.12: Spectrogram of a type 4 test; steady-state conditions with a controlled excitation ramp from 1000 to 6000 Hz.	116
Figure 6.13: Spectrogram of Figure 6.12, viewed up to 40,000 Hz, with excitation signal overtones indicated.	117
Figure 6.14: Spectrogram from a 60 bar test illustrating transitioning LF chugging during transverse mode excitation.	118
Figure 6.15: Dynamic pressure signal during ramped excitation of the 1L, 1T and 1L1T modes. The calculated acoustic pressure amplitude is overlaid (red line). The ramped excitation frequency (blue line) is also overlaid for information.	119
Figure 6.16: Spectrogram of the <i>PCCdyn2</i> signal from an early test with uncontrolled excitation ramp.	121
Figure 6.17: Progression of acoustic pressure amplitude during 1T mode excitation for a cold-flow test without combustion (a), and a hot-fire test at 60 bar with GH ₂ (b).	122
Figure 6.18: Spectrogram showing ramped excitation of the 1T and 1L1T modes for a 40 bar test with LH ₂	123
Figure 6.19: Combustion chamber and injection manifold acoustic spectra during peak 1T-mode resonance amplitude from the 40 bar test with LH ₂ in Figure 6.18.	125
Figure 6.20: Combustion chamber and injection manifold acoustic spectra during off-resonance excitation from the 40 bar test with LH ₂ in Figure 6.18.	125
Figure 6.21: FE model results for acoustic modes of the H ₂ injector (left column) and the LOx injector (right column).	127
Figure 7.1: Instantaneous OH* emission image, shown in false-colour (a), and corresponding shadowgraph image (b), during off-resonance conditions.	132
Figure 7.2: Time-averaged shadowgraph (a) and OH* emission (b) images during off-resonance conditions in a 60 bar test with GH ₂	133
Figure 7.3: Time-averaged OH* emission images during off-resonance conditions in 40 bar, LH ₂ test A (a), and in 40 bar, LH ₂ test B (b).	133
Figure 7.4: Time-averaged shadowgraph (a) and OH* emission (b) images during 1T mode excitation with $p/P_{cc} = 7.4\%$	133
Figure 7.5: Projected cross-section of the flames from the 40 bar test with LH ₂ , case A.	134
Figure 7.6: Projected cross-section of the flames from the 40 bar test with LH ₂ , case B.	134
Figure 7.7: Example sequence of images used to measure transverse (i.e. vertical) displacement of the flame during 1T-mode excitation. The raw OH* image (upper row) and its converted binary counterpart (lower row) are shown.	136
Figure 7.8: Comparison of transverse flame displacement measurements and acoustic particle displacement signals.	137
Figure 7.9: Spectrogram of mean OH* emission from high-speed imaging at 40 bar with LH ₂ , case B.	138
Figure 7.10: Spectrogram of mean OH* emission from high-speed imaging at 40 bar with GH ₂	139
Figure 7.11: Spectrogram of mean OH* emission from high-speed imaging at 60 bar with GH ₂	139
Figure 7.12: Spectrogram of photomultiplier signal at 40 bar with GH ₂	140
Figure 7.13: Spectrogram of photomultiplier signal at 60 bar with GH ₂	141
Figure 7.14: Reconstructed acoustic pressure and velocity distributions of the 1T mode used for the calculation of Rayleigh indices; (a) at the point of peak acoustic pressure for <i>PCCdyn2</i> (a), and one-quarter of a cycle later at the point of peak velocity amplitude (b).	143
Figure 7.15: Response of the flame to 1T mode resonance comparing time-averaged distributions of the raw OH* images (a), the pressure based Rayleigh index (b), the velocity based Rayleigh index (c), acoustic pressure phase (d), and acoustic velocity phase (e).	144
Figure 7.16: Sequence of raw OH* images (upper row) and band-pass filtered emission distribution (lower row) illustrating how transverse (up and down) convective motion results in artefact signals in band-pass images. Two example frame sequences are given from excitation of the 1T mode at 4350 Hz.	145
Figure 7.17: Reconstructed acoustic pressure and velocity distributions of the 1L mode used for the calculation of Rayleigh indices; at the point of peak acoustic pressure in the window (a), and one-quarter of a cycle later at the point of peak velocity amplitude (b). The velocity antinode is located downstream of the window.	146
Figure 7.18: Response of the flame to 1L mode resonance comparing time-averaged distributions of the raw OH* images (a), the pressure-based Rayleigh index (b), the velocity-based Rayleigh index (c), acoustic pressure phase (d), and acoustic velocity phase (e).	148
Figure 7.19: Response factor distribution for coupling of OH* emission with acoustic pressure during 1L-mode resonance in tests at 60 bar with GH ₂ , cases A (a) and B (b).	148
Figure 7.20: Response factors for coupling of OH* emission with acoustic pressure during 1L-mode resonance.	149
Figure 8.1: Example instantaneous shadowgraph image (a) and corresponding instantaneous OH* emission image, shown in false colour (b), for a 60 bar test with GH ₂	156
Figure 8.2: Natural LOx core breakup behaviour at 60 bar with GH ₂	157
Figure 8.3: Map of shear-coaxial breakup regimes defined by Chigier and Reitz (1995).	158
Figure 8.4: Coaxial air and liquid injection with breakup in the fibre-type regime (Chigier & Reitz 1995, p.120).	158

Figure 8.5: Comparison of shadowgraph images for subcritical (40 bar) and supercritical (60 bar) chamber pressures, from tests at 40 bar with GH ₂ (a), 60 bar with GH ₂ (b), 40 bar with LH ₂ (c), and 60 bar with LH ₂ (d).....	160
Figure 8.6: Critical mixing lines of common binary systems (Mayer & Smith 2004, p.8)	161
Figure 8.7: Surface tension of the oxygen/hydrogen binary system (Mayer & Smith 2004, p.8)	161
Figure 8.8: Time-averaged shadowgraph (upper row) and OH* emission images (lower row) during off-resonance excitation (a), and 1T-mode excitation with $p/P_{cc} = 7.4\%$ (b).....	162
Figure 8.9: Sequential shadowgraph images from a 60 bar test with GH ₂ , recorded at 20,000 fps during 1T mode excitation with $p/P_{cc} = 7.4\%$	163
Figure 8.10: Major steps in the semi-automated core detection routine; the binary image created following pre-processing with the user-specified analysis area (a), the intact core centreline (b), and the centerline overlaid on the raw image (c).....	165
Figure 8.11: Acoustic pressure signals and shadowgraph recording durations for 60 bar, GH ₂ case A (a), and case C (b), with shadowgraph recording rates of 7000 fps and 20,000 fps, respectively.	165
Figure 8.12: Frame-by-frame measurements of the intact LOx core length from 5-ms duration (100-frame) samples from the case C test at 60 bar with GH ₂ . The first sample is from the beginning of the shadowgraph recording in.....	167
Figure 8.13: Normalised intact core length (L/D) plotted against relative acoustic pressure amplitude (p/P_{cc}).....	168
Figure 8.14: Normalised intact core length (L/D) plotted against the ratio of transverse-acoustic to H ₂ -injection momentum flux.....	169
Figure 8.15: Normalised intact core length (L/D) plotted against transverse acoustic Weber number.	169
Figure 8.18 Comparison of break-up regime transitions for LOx in dry air and helium under 30 bar (Vieille, Chauveau & Gokalp 1999).....	173
Figure 8.19 Experimental data and the corresponding transition criteria for liquid oxygen droplet breakup regimes (Vieille, Chauveau & Gokalp 1999).....	173
Figure A.1: Twin resonator segment concept with square resonator (internal geometry)	189
Figure A.2: Concepts for internal geometry at the resonator chamber intersection.....	190
Figure A.3: Dimensions of twin resonator chamber internal geometry.	190
Figure A.4: Estimated flow pattern near the resonator-chamber intersection	191
Figure A.5: Meshed model of the TRS for CFD analysis.	192
Figure A.6: Velocity field results for CFD Case 1.....	193
Figure A.7: Velocity field results for CFD Case 2.....	193
Figure A.8: Velocity field results for CFD Case 3.....	194
Figure A.9: Individual jet streamlines for CFD Case 3.	194
Figure A.10: Concept for secondary hydrogen injection	195
Figure A.11: Secondary injection CFD model geometry.....	196
Figure A.12: CFD streamline results comparison for TRS secondary injection.	196
Figure A.13: CFD calculated gas temperature distribution for the TRS with secondary H ₂ injection.....	196
Figure A.14: Acoustic mode comparison for TRS with and without secondary H ₂	197
Figure A.15: TRS heat load with and without secondary H ₂ injection.....	198
Figure A.16: Acoustic mode shapes with nitrogen injection.....	198
Figure A.17: Example numerical acoustic pressure distributions for the TRS, with and without pooled water condensate. ...	199
Figure B.1: Overview of the internal volumes of BKH.....	201
Figure B.2: Dimensions of the internal volumes of BKH	202
Figure B.3: Detailed BKH injector dimensions.....	203
Figure B.4: Locations of sensors in BKH.	204
Figure C.1: A photograph of the round secondary nozzle (a), and the corresponding excitation profile (b).....	205
Figure C.2: A photograph of the secondary nozzle with double sine profile (a), and the corresponding excitation profile (b).....	206
Figure C.3: Comparison of acoustic pressure spectra in the combustion chamber for excitation with the round and sine-profiled secondary nozzles. Spectra are shown for stationary, off-resonance excitation (a), and for ramped, off-resonance excitation (b).....	207

List of tables

Table 1: Typical specific impulse for chemical rocket types.	8
Table 2: Specific impulse for bipropellant combinations.	11
Table 3: Critical properties of oxygen and hydrogen.	13
Table 4: Theoretical mode frequencies for basic chamber dimensions of BKH.	72
Table 5: BKH injector design parameters.	73
Table 6: FE calculated mode frequencies for BKH with and without secondary nozzle installed.	114
Table 7: Summary of measured acoustic pressure amplitudes for various BKH configurations and excitation conditions. ...	119
Table 8: Injection parameters for studies of flame response.	131
Table 9: Injection parameters for tests with shadowgraph imaging.	155
Table 10: Gas properties and correlating ratios for three different types of atmospheres surrounding LOx droplets in the reacting coaxial spray.	172

Glossary

Nomenclature

A	Area	LOx	Liquid oxygen
β^*	Reduced acoustic admittance	\dot{m}	Mass flow rate
c	Sound speed	M	Molecular mass, g/mol
c^*	Characteristic exhaust velocity	M_{bulk}	Bulk flow Mach number
c_p	Specific heat capacity	n	Mode index
CH ₄	Methane	N	Response factor
D	Diameter	N ₂	Nitrogen
η_{c^*}	Characteristic exhaust velocity efficiency	O ₂	Oxygen
f	Frequency	p	Pressure
F	Thrust	p'	Acoustic pressure
g_0	Standard gravitational acceleration, 9.8 m/s ²	P_{cc}	Combustion chamber pressure
GH ₂	Gaseous hydrogen	\dot{q}	Heat release rate
GN ₂	Gaseous nitrogen	ρ	Density
GOx	Gaseous oxygen	R_p	Rayleigh index based on acoustic pressure
γ	Ratio of specific heats	R_u	Rayleigh index based on acoustic velocity
H ₂	Hydrogen	ROF	Oxidiser-to-fuel mixture ratio
I	OH* emission intensity	t	Time
I_{sp}	Specific impulse	T	Temperature
J	Momentum flux ratio	u	Velocity
L	Length	u'	Acoustic particle velocity
LH ₂	Cryogenic ('liquid') hydrogen	VR	Inner-to-outer-propellant injection velocity ratio
LN ₂	Liquid nitrogen		

Subscripts

<i>bulk</i>	Bulk, total
<i>cc</i>	combustion chamber
<i>crit</i>	Critical therophysical property
<i>d</i>	Droplet (of LOx)
<i>H</i>	Hydrogen (fuel)
<i>MN</i>	Main (exhaust) nozzle
<i>O</i>	Oxygen (oxidiser)
<i>SN</i>	Secondary (exhaust) nozzle
<i>x</i>	x-axis direction
<i>y</i>	y-axis direction
<i>z</i>	z-axis direction

Acronyms

CFD	Computational Fluid Dynamics
CNRS	National Scientific Research Centre (France)
DLR	German Aerospace Center
FEA	Finite Element Analysis
IRPHE	Research Institute for Equilibrium Systems (France)
ONERA	National Aerospace Lab (France)
NASA	National Aeronautics and Space Administration

Abstract

Self-sustaining pressure oscillations in the combustion chamber, or combustion instability, is a commonly encountered and potentially damaging phenomenon in liquid propellant rocket engines (LPREs). In the high-frequency variety of combustion instability, the pressure oscillations in the combustion chamber take on the form and frequency of an acoustic resonance mode of the combustion chamber volume. The most common mode in naturally occurring instability, and also the most destructive, is the first tangential mode, with acoustic gas oscillations oriented transversally to the direction of propellant injection. The instability is driven by the coupling between acoustic oscillations and unsteady energy release from combustion. The mechanisms through which injection and combustion firstly respond to the acoustic field, and secondly feed energy back into the acoustic field have not yet been fully characterised.

Shear coaxial-type injectors are common in LPREs. Past experimental and numerical research efforts have investigated the interaction between this type of injector and transverse acoustic fields. Some experimental efforts have successfully forced transverse acoustic modes and studied their influence on shear coaxial injection under LPRE-like conditions. Acoustic forcing of coaxially injected LOx/H₂ has previously been conducted only at low pressures and injection performance levels. This work addresses the lack of experimental data available for the interaction of shear coaxial injection of LOx/H₂ with acoustics under conditions representative of industrial engines.

A new experimental rocket combustor, designated 'BKH', was developed for investigating the response of a reacting spray of coaxially injected LOx/H₂ to an acoustic field. For characterising the response, simultaneous high-speed recordings of both backlit shadowgraph and hydroxyl radical (OH*) chemiluminescence imaging have been captured through optical access windows. The operating conditions of BKH extend to conditions more representative of actual LPREs than has previously been achieved with LOx/H₂ in studies of flame-acoustic interaction. BKH was run at pressures of 40 or 60 bar, which correspond to subcritical and supercritical thermo-physical regimes for oxygen. Hydrogen injection temperature was ambient, around 290 K, or cryogenic, around 50 K. An array of multiple injectors was used to better represent real engines. A system for modulating the nozzle exhaust flow was used to induce acoustic perturbations inside the combustion chamber. Two types of perturbation were applied to the near-injection region; oscillating acoustic pressure, and oscillating transverse acoustic velocity.

BKH was used to investigate how subcritical or supercritical pressure level and ambient or cryogenic hydrogen injection temperature influence the interaction of acoustic pressure or velocity with injection and combustion processes. Shadowgraph imaging reveals up to 70% reduction in the length of the oxygen jet when subjected to acoustic velocity of amplitude approaching that of the hydrogen injection velocity. Furthermore, the mode of jet breakup changes from its natural growth-and-detachment behaviour to a 'transverse stripping' mechanism. OH* imaging reveals a corresponding decrease in the extent of the flame, and increase in emission intensity. When subjected to acoustic pressure, OH* emission from the flame was observed to fluctuate in phase with pressure. Thus, responses to both acoustic pressure and velocity have been observed in BKH, which together may form the basis of a coupling mechanism for driving natural combustion instability in LPREs.

Declaration of originality

I certify that this work contains no material which has been accepted for the award of any other degree or diploma in any university or other tertiary institution and, to the best of my knowledge and belief, contains no material previously published or written by another person, except where due reference has been made in the text. In addition, I certify that no part of this work will, in the future, be used in a submission for any other degree or diploma in any university or other tertiary institution without the prior approval of the University of Adelaide and where applicable, any partner institution responsible for the joint-award of this degree.

I give consent to this copy of my thesis, when deposited in the University Library, being made available for loan and photocopying, subject to the provisions of the Copyright Act 1968.

I also give permission for the digital version of my thesis to be made available on the web, via the University's digital research repository, the Library catalogue and also through web search engines, unless permission has been granted by the University to restrict access for a period of time.

Justin S. Hardi

June 2012

Acknowledgements and disclaimer

First and foremost I would like to thank my supervisors, A/Prof Bassam Dally and Prof Michael Oswald. Their guidance was invaluable, and their expertise and patience were an endless source of inspiration. A special mention must also be made of Dr Gerald Schneider who made it possible for me to leave little old Adelaide for the exciting world of aerospace in Europe.

I am indebted to Dimitry Suslov and Bernhard Knapp for their additional valued guidance.

For their collaboration in development of the BKH combustor, I would like to thank Gerhard Krühsel and the Engineering department, especially David Hladik. Thanks also to all personnel of the M10 and M29 workshops, to M3 technicians Michael Zepmeisel and Markus Dengler, and to Andreas Märklen for their expertise in hardware preparation. Philipp Groß and the P8 Test Facility team are acknowledged for their professional efforts in test operations. Thanks to Walter Clauß for the design and operation of optical diagnostics.

I wish to express my gratitude to my fellow students who assisted me over the course of the project; Samuel Webster, Scott Beinke, Harvey Camilo Gomez Martinez, Jannis Schücker, Maike Neuland and Filip Dimoski. I hope you learned as much from me as I did from all of you.

To my colleagues and good friends Michele Negri, Stefan Gröning, and all the Wohnheimers who made coming to work so enjoyable, as well as life in Möckmühl, cheers!

Finally, I owe my deepest gratitude to my family and to Katharina Wirth for their love and support.

Research undertaken for this report has been assisted with a grant from the Smith Fund (www.smithfund.org.au). The support is acknowledged and greatly appreciated.

The Smith Fund by providing funding for this project does not verify the accuracy of any findings or any representations contained in it. Any reliance on the findings in any written report or information provided to you should be based solely on your own assessment and conclusions. The Smith Fund does not accept any responsibility or liability from any person, company or entity that may have relied on any written report or representations contained in this report if that person, company or entity suffers any loss (financial or otherwise) as a result.



THE SIR ROSS & SIR KEITH SMITH FUND